Assessing the contamination of SuperDARN global convection maps by non-F-region backscatter

G. Chisham, M. Pinnock

Annales Geophysicae (2002) 20: 13–28 © European Geophysical Society 2002

Annales Geophysicae

Assessing the contamination of SuperDARN global convection maps by non-F-region backscatter

G. Chisham and M. Pinnock

British Antarctic Survey, Natural Environment Research Council, High Cross, Madingley Road, Cambridge, CB3 0ET, UK

Received: 13 February 2001 – Revised: 3 September 2001 – Accepted: 10 September 2001

Abstract. Global convection mapping using line-of-sight Doppler velocity data from the Super Dual Auroral Radar Network (SuperDARN) is now an accepted method of imaging high-latitude ionospheric convection. This mapping process requires that the flow measured by the radars is defined solely by the convection electric field. This is generally only true of radar backscatter from the ionospheric F-region. We investigate the extent to which the E-region and ground backscatter in the SuperDARN data set may be misidentified as F-region backscatter, and assess the contamination of global convection maps which results from the addition of this non-F-region backscatter. We present examples which highlight the importance of identifying this contamination, especially with regard to the mesoscale structure in the convection maps.

Key words. Ionosphere (plasma convection) – Radio science (radio wave propagation; instruments and techniques)

1 Introduction

Measurements of plasma convection in the high-latitude ionosphere provide an insight into processes which affect the dynamics of the large-scale magnetospheric convection electric field (e.g. dayside and nightside reconnection, and viscous processes on the magnetopause). Hence, studying high-latitude convection is an important way of probing the nature of the solar wind magnetosphere-ionosphere interaction. Global convection mapping using data from the Super Dual Auroral Radar Network (SuperDARN), as pioneered by Ruohoniemi and Baker (1998), is fast becoming a significant tool for imaging high-latitude ionospheric convection. This method has been used to study the large-scale global nature of convection (Amm et al., 1999; Shepherd et al., 1999; Shepherd and Ruohoniemi, 2000), and it is increasingly being used to study local, mesoscale variations (Yeoman et al., 2000; Huang et al., 2000), and transient features (Greenwald et al., 1999; Neudegg et al., 2000) of the ionospheric convection pattern.

SuperDARN is a network of coherent scatter HF radars (Greenwald et al., 1995) which measure backscatter from field-aligned decametre scale ionospheric irregularities. The radars transmit HF signals which are refracted toward the horizontal as they enter ionospheric regions with higher electron concentrations. If these regions contain irregularities, then the radar signals are backscattered when the HF signal wave vector is perpendicular to the magnetic field (i.e. perpendicular to the irregularities). In the high-latitude ionosphere, these irregularities are often present (Tsunoda, 1988). At F-region altitudes, they move with the background plasma drift (Villain et al., 1985; Ruohoniemi et al., 1987; Eglitis et al., 1998; Davies et al., 1999) and thus provide information about large-scale convection and related processes in the radar field of view. The SuperDARN radars are, therefore, a very good diagnostic tool for studies of magnetosphere-ionosphere coupling.

Each SuperDARN radar consists of a main array of 16 log-periodic antennae, which both transmit and receive HF signals, and which provide echo location in the horizontal plane. Many of the radars also employ an interferometer array of 4 antennae with receive capability only, in order to determine the vertical angle of arrival of the echoes. The radars transmit signals at a fixed frequency in the range of 8–20 MHz, and from the return signals an estimate of the variation in backscatter power, line-of-sight Doppler velocity (V_{los}), and spectral width (Δv) in the radar field of view is derived (see e.g. Baker et al., 1995 or Barthes et al., 1998 for details). Many of the SuperDARN radars have overlapping fields of view, which also allow for the estimation of unambiguous field-perpendicular ($\sim$horizontal) velocity vectors (via the "merge" technique) (Cerisier and Senior, 1994). However, although the SuperDARN radars typically have good backscatter rates, the extent of overlapping backscatter is often limited. To fully utilise all the available data, other techniques are often employed to image ionospheric convection on a large scale. One such technique is SuperDARN

Correspondence to: G. Chisham (G.Chisham@bas.ac.uk)

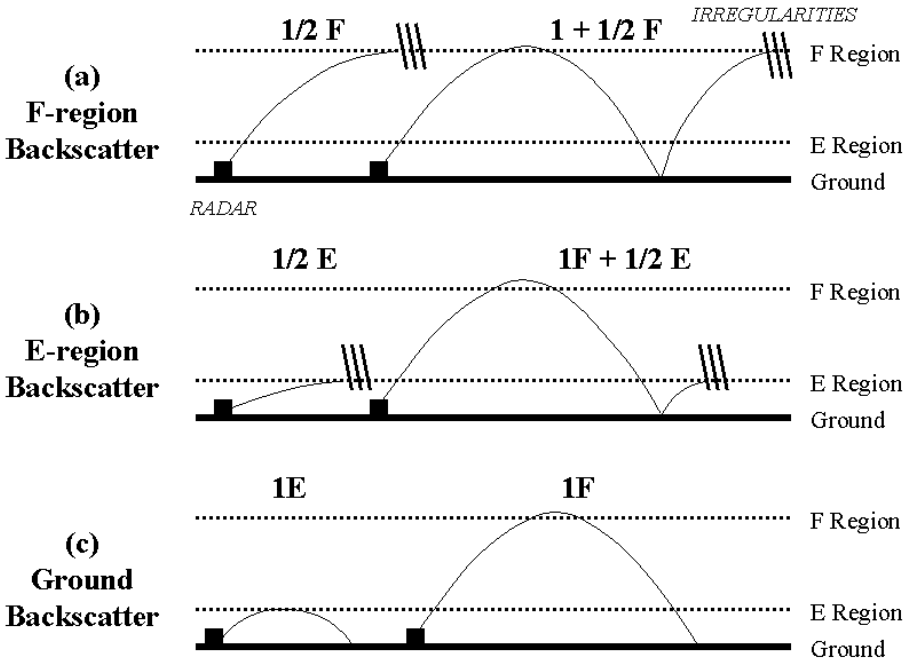

Fig. 1. Schematic diagram representing the typical propagation modes of SuperDARN HF radar signals backscattered from **(a)** F-region irregularities, **(b)** E-region iregularities, and **(c)** the ground.

global convection mapping.

SuperDARN global convection maps are produced by fitting line-of-sight velocity data from the SuperDARN radars to an expansion of an electrostatic potential function expressed in terms of spherical harmonics. The mapping technique consists of two distinct stages: (1) the gridding of the line-of-sight velocity data, and (2) the least-squares fitting of the gridded data. The gridding process represents preprocessing of the data into a form that is more conducive to the fitting. First, line-of-sight velocity data flagged by the raw data processing as ground backscatter (i.e. non-ionospheric echoes, typically those for which both $|V_{los}| < 30$ m/s and $\Delta v < 35$ m/s) are removed. The remaining line-of-sight velocity data are spatially and temporally median filtered to remove noise from the data set and increase the statistical reliability of the data. These data are then mapped onto an equal area geomagnetic coordinate grid (see Ruohoniemi and Baker, 1998 for full details). The gridded velocity data are assigned a weighting that depends on the velocity uncertainty within the grid cell; a grid cell with a high velocity uncertainty will be given a low weighting. The gridded velocity data from all the available SuperDARN radars in the relevant hemisphere are then combined. In order to constrain the solution effectively in the regions where little or no data are available, the data are augmented by velocity vectors from a statistical model (typically that of Ruohoniemi and Greenwald, 1996). The choice of statistical model is usually based on the prevailing IMF conditions and generally has little influence on the solution in the regions where good data exist (Shepherd and Ruohoniemi, 2000).

In the next stage of the analysis, the fitting is performed on the combined gridded velocity data and the best fit determined by a least-squares method. The fitting is dependent on two user-selected parameters; (1) the order of the spherical harmonic fit, and (2) the spatial extent over which the fit is performed (i.e. the latitudinal and local time extent of the convection zone). Mesoscale ($\sim 10^3$ km) features of the convection are reproduced better by higher order fits and thus the uncertainty of the fit is reduced. However, high order fits are more computationally intensive. Changing the spatial extent of the fit can change the global nature of the solution, but rarely has a significant effect on mesoscale variations. The solution provides an estimate of the convection electric field across the polar regions of the ionosphere and can be used to study its large-scale characteristics (e.g. the cross-polar cap potential Shepherd and Ruohoniemi, 2000) or its mesoscale features (e.g. flow vortices, convection reversal boundaries). Small-scale ($\sim 10^2$ km) features are typically blurred by the spatial and temporal averaging process and hence, this technique is generally not suitable for small-scale studies.

Global convection mapping is proving an important technique for imaging high-latitude ionospheric convection. However, as with all convection studies, problems can arise in the mapping process since not all of the backscatter measured by the SuperDARN radars arises from F-region irregularities moving under the influence of the convection electric field. The HF radar signals can be backscattered from irregularities in the ionospheric E-region or from the ground (after reflection by the ionosphere), and it is not always a trivial task to determine the exact source of the backscatter. The SuperDARN data set can also, on occasion, contain significant noise or interference. The characteristics and lo-

cation of SuperDARN backscatter are dependent on many factors, including the seasonal and diurnal changes in the E- and F-region electron concentrations, and the signal frequencies employed (Villain et al., 1984; Milan et al., 1997b; Ruohoniemi and Greenwald, 1997). Figure 1 presents a schematic diagram illustrating some of the typical propagation modes which result in HF backscatter. Figure 1a describes the propagation modes where the signal backscatters from irregularities in the ionospheric F-region. The two modes shown represent $\frac{1}{2}$ hop and $1\frac{1}{2}$ hop propagation paths. Further multiple hop modes ($2\frac{1}{2}$ hop, $3\frac{1}{2}$ hop, etc.) are possible but contribute little to most data sets due to increasing signal attenuation over longer propagation paths. For F-region backscatter the measured line-of-sight velocity relates exclusively to the $\boldsymbol{E} \times \boldsymbol{B}$ drift of the ionospheric plasma under the influence of the convection electric field.

Figure 1b describes the propagation modes where the signal backscatters from irregularities in the ionospheric E-region. The two modes shown represent $\frac{1}{2}$ hop and $1\frac{1}{2}$ hop propagation paths, similar to the F-region examples; hence, E-region backscatter can be observed at both near and far ranges. The bulk of the E-region backscatter can be classified into two types (I and II), which relate to the instability mechanism responsible for the ionospheric irregularities from which the signal has scattered (Fejer and Kelley, 1980; Haldoupis, 1989). In the F-region, both the ion and electron distributions move under the influence of the convection electric field. However, the higher ion-neutral collision frequency in the E-region means that the ions are constrained to the neutral flow speed. The resulting differential flow between the ions and electrons gives rise to the two-stream (or Farley-Buneman) instability (Farley, 1963; Buneman, 1963), which results in the observation of type I Doppler spectra in the backscattered signal. Type I spectra are characterised by a low spectral width and a Doppler velocity which is constrained to be near the local ion-acoustic speed, C_S (C_S ~350–400 m/s at 110 km altitude). The Doppler velocity of this type I backscatter underestimates the plasma drift velocity (Nielsen and Schlegel, 1983) and hence, can introduce inaccuracy in convection studies. Type II Doppler spectra represent backscatter from E-region irregularities created by the gradient-drift instability (Ossakow and Chaturvedi, 1979) and these spectra provide a true estimate of the convection flow speed.

The ranges at which $\frac{1}{2}$ hop E- and F-region backscatter can be received are conditioned by the vertical radiation pattern of the transmitting antennae. This pattern has a peak at an elevation angle above the horizontal of ~15–30° (depending on the HF signal frequency). The lack of high elevation angle rays (e.g. above ~45°) means that under most conditions, it is difficult to receive $\frac{1}{2}$ hop F-region backscatter at ranges less than ~600 km. Below this range, all echoes are typically $\frac{1}{2}$ hop E-region backscatter. Similarly, the lack of low elevation angle rays (e.g. below 10°) means that under most conditions, it is difficult to receive $\frac{1}{2}$ hop E-region backscatter at ranges above ~600 km.

Figure 1c describes the propagation modes where the transmitted signal backscatters from the ground due to the roughness of the Earth or ocean surface. The two modes shown represent 1 hop propagation paths, the first refracting in the E-region, the second in the F-region. Ground backscatter is often easily identified in the radar data sets since it typically has a near-zero velocity and a low spectral width. The SuperDARN raw data processing flags all data points suspected of being ground backscatter (those for which $|V_{los}| < 30$ m/s and $\Delta v < 35$ m/s) so that they can be easily removed in convection studies. However, problems can arise when the measured backscattered signal represents a combination of several sources, e.g. a mixture of ground and ionospheric backscatter from different propagation modes. The SuperDARN raw data processing assumes that the backscattered signal consists of a single source and hence, multiple sources can lead to erroneous values of velocity and spectral width. Barthes et al. (1998) discuss this possibility in detail and have shown that a combination of ground backscatter (with $V_{los} \sim 0$ and low Δv) and ionospheric backscatter (with high V_{los} and high Δv) can be misidentified as ionospheric backscatter with low velocity (~0 m/s) but high spectral width. These data would not be identified as ground backscatter by the raw data processing and hence, represent a possible source of contamination in SuperDARN global convection maps.

It is important in convection studies to identify what measurements describe the motion of plasma moving exclusively under the influence of the convection electric field and assess the impact of those measurements which do not (e.g. noise, interference, and the ground and type I E-region backscatter discussed above). Discriminating between the sources of regions of backscatter can be a difficult process. Interferometric measurements allow for the determination of the elevation angle of arrival of the backscattered signal (Milan et al., 1997a; André et al., 1998). Measurements of the elevation angle allow for the estimation of the altitude of the scattering irregularities and can help to distinguish between ground, E- and F-region backscatter. However, interpretation of elevation angle information requires caution: (1) Elevation angle measurements can often be highly ambiguous due to the multitude of different radio wave propagation modes which can exist under different ionospheric conditions; (2) Without accurate ionospheric models, the elevation angle information can only be used assuming direct (line-of-sight) ray paths. The ray tracing work of Villain et al. (1984) showed that, in reality, a variety of propagation modes are possible for a given set of transmission characteristics. The resulting ambiguity can lead to an erroneous determination of propagation paths and scattering altitudes; (3) Good quality interferometer measurements are not always achieved due to the lower gain of the interferometer array. These issues highlight the fact that interferometer data alone cannot always be used to resolve ground, E- and F-region backscatter. This paper will discuss methods of estimating backscatter origin.

Once contaminating backscatter has been identified, one approach is to remove it completely from the data set. The

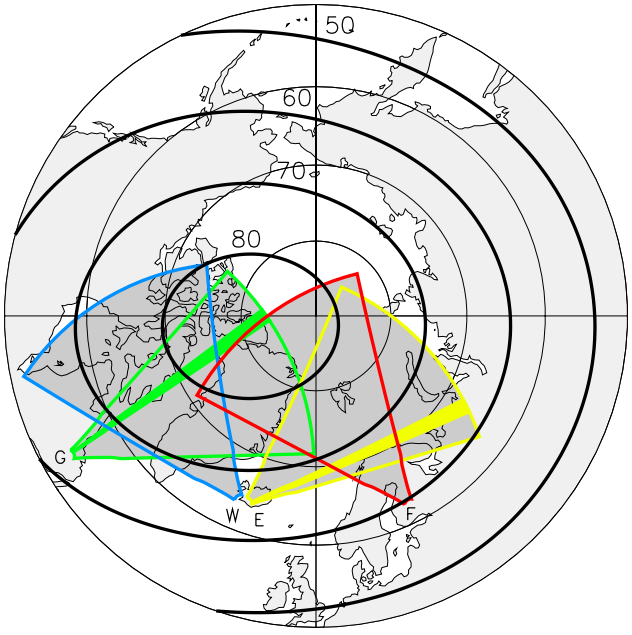

Fig. 2. Fields of view of four of the Northern Hemisphere SuperDARN radars (Goose Bay (G), Iceland West (W), Finland (F), and Iceland East (E)). The shaded beams represent Goose Bay beam 4 (Green) and Iceland East beam 13 (Yellow). The bold lines represent lines of constant AACGM latitude (values as shown).

global convection mapping technique deals very well with noise and interference in the data; this is removed (or given a very low weighting) by the median filtering in the gridding process. The technique also deals fairly well with ground backscatter. All ground backscatter flagged by the SuperDARN raw data processing is removed. As discussed above, this flagging is often inadequate and ground backscatter can remain, especially that which results from a combination of propagation modes. However, the mapping process also allows for the removal of all backscatter with an absolute line-of-sight velocity below a chosen value (the default velocity is 35 m/s), to remove any remaining ground backscatter which has been erroneously flagged as ionospheric backscatter. We will discuss the effectiveness of the default processing later in this paper. At present, the global convection mapping technique has no way of dealing with any contaminating E-region backscatter.

We should also highlight that these problems are not exclusive to the global convection mapping technique, but apply to all SuperDARN convection studies. This backscatter contamination is also a potential problem when determining convection velocity vectors in regions of overlapping backscatter from two radars using the "merge" technique. Understanding the nature of the backscatter in these studies is obviously important for a correct interpretation of the data.

The purpose of this paper is twofold: first, to determine the extent of E-region and ground backscatter contamination in SuperDARN data, and second, to determine an efficient way to remove this backscatter on a routine basis in order to produce more reliable estimates of the convection electric field via SuperDARN global convection mapping.

2 Statistical backscatter distributions

In order to evaluate potential sources of backscatter contamination, we have determined statistical distributions of backscatter measured by beams in some of the Northern Hemisphere radars. A year's worth of data (from 1998) was employed to determine the typical backscatter distributions for selected beams from four of the radars. Figure 2 illustrates the fields of view of these radars (Goose Bay (G), Iceland West (W), Finland (F), and Iceland East (E)). The bold lines represent contours of constant latitude in the AACGM coordinate system. Both zonal and meridional pointing beams were studied. Only data from SuperDARN common mode intervals were used in the compilation of the database to provide some consistency between the radar observations. In the common mode, each radar measures in 16 beam directions, with each beam consisting of 75 range gates with a pulse length of 300 μs (giving 45 km range resolution) and a lag to first range of 1200 μs (180 km), giving a far range limit of $\sim$3500 km. Data flagged as ground backscatter by the SuperDARN raw data processing were removed during the compilation of the database, as were data with a velocity error $>$200 m/s (these are defaults employed by the global convection mapping technique). Only two examples of the resulting backscatter distributions will be presented here (from the SuperDARN radars at Iceland East (CUTLASS Iceland) and Goose Bay). However, these observations highlight the important features which were characteristic of all the radars.

2.1 Example zonal beam

Iceland East beam 13 points eastward and is approximately L-shell aligned ($\sim$65°- 68° AACGM latitude), representing a good example of a zonal beam (shown as a shaded yellow beam in Fig. 2). Figure 3a presents the occurrence distribution of velocity measurements from this beam, as well as the distribution in range gate-velocity space, for all of 1998. For this figure and following figures of this type, the velocity occurrence distribution is plotted on a logarithmic scale and the occurrence contours in the range gate-velocity distribution are also on a logarithmic scale. Negative line-of-sight velocities represent flow away from the radar, whereas positive line-of-sight velocities represent flow toward the radar. The velocity distribution in Fig. 3a displays a peak at zero, although a series of other peaks are clearly visible in the data (at approximately $-$1350, $-$1150, $-$850, $-$700, $-$450, 450, 700, 850, 1150, and 1350 m/s). Figure 3b presents the same Iceland East beam 13 velocity distribution but here, the contour map displays the distribution in magnetic local time-velocity space. A close study of Figs. 3a and 3b reveals that a number of distinct backscatter distributions characterise this beam. First, the largest distribution of points are centred

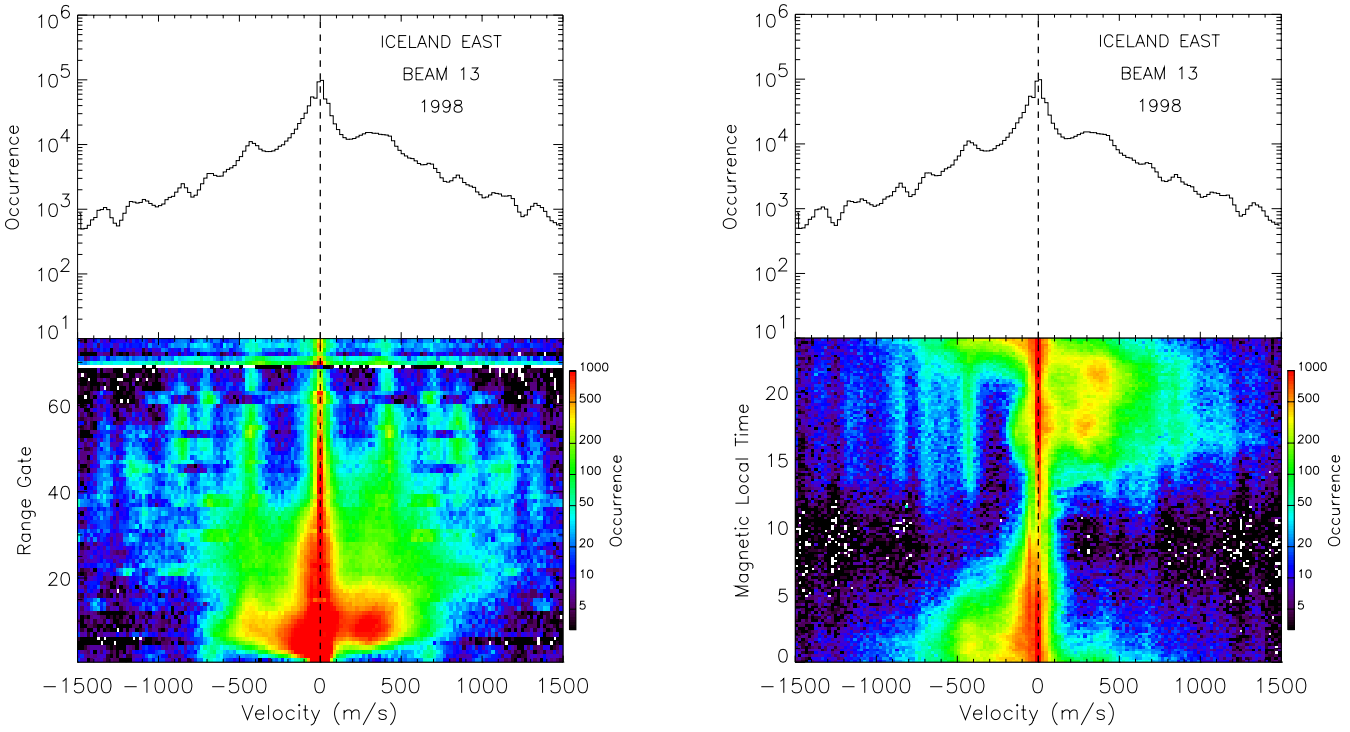

Fig. 3. Line-of-sight velocity distributions from Iceland East beam 13 for the whole of 1998. Additionally shown are **(a)** the distribution in range gate-velocity space, and **(b)** the distribution in magnetic local time-velocity space. Positive line-of-sight velocities represent the flow toward the radar, whereas negative line-of-sight velocities represent the flow away from the radar.

around zero at low to mid-ranges. This distribution is evident at almost all magnetic local times and most likely represents the observation of near-corotation flows in the E- and F-regions. At far ranges, the distribution around zero becomes much narrower and is highly symmetric about zero, which is suggestive of a ground backscatter distribution. Changing the resolution on the contour plots (not shown) shows that this ground backscatter distribution is also significant at lower ranges on top of the low velocity distribution. This suggests that the SuperDARN raw data processing has not been successful in identifying all the ground backscatter in the data set. However, the bulk of the ground backscatter distribution that remains appears to occur for $V_{los} < 35$ m/s, which means that it is removed by default in the gridding stage of the global convection mapping process.

Second, there is a large distribution of backscatter with low velocities (<700 m/s) at low ranges. This distribution most likely represents return flows in the twin cell convection pattern. The distribution has a peak in the dusk sector (∼15:00–24:00 MLT), which corresponds to observations of the dusk-side return flow in the global convection system. There is a smaller peak in the dawn sector (∼23:00–06:00 MLT), which corresponds to the dawnside return flow. This is ionospheric backscatter which is related to the convection electric field.

Third, there are a series of peaks in the distribution at discrete velocities, most evident at far ranges. These peaks occur most strongly, at all ranges, for velocities $\sim \pm 400$ m/s. The sharp, discrete nature of these peaks suggest that they represent type I E-region backscatter that is constrained to be close to the ion-acoustic speed. These peaks are confined predominantly to the afternoon and evening sectors (∼12:00–24:00 MLT) and are also characterised by low spectral widths (not shown). The extent of type I E-region backscatter in the Iceland East data set, in both near and far range backscatter, has been highlighted previously by Milan et al. (1997b), and Milan and Lester (1998). There are also a number of other discrete velocity peaks at $\sim \pm$ 700, 850, 1150, and 1350 m/s which occur at similar ranges and magnetic local times as the type I backscatter. These peaks may represent signal interference which manifests itself at discrete velocities, although it is also possible that they have a physical ionospheric origin. They may represent the rarely observed type IV E-region backscatter (Fejer et al., 1984), which has been shown to occur at discrete velocity peaks above the ion-acoustic speed (Haldoupis et al., 1991, 1993). The origin of this type IV backscatter is still a matter of debate (Farley et al., 1991; St.-Maurice et al., 1994; Prikryl et al., 1995). Whatever the source is of these peaks in the distribution, this backscatter is unlikely to result from irregularities moving solely under the influence of the convection electric field and hence, forms another potential source of contamination in global convection maps. We should also comment that very little of the backscatter at ranges further than range gate 40, in Fig. 3a, appears convection related, but rather it appears to be predominalty ground and E-region backscatter. This was also the case for other zonally-directed

beams.

2.2 Example meridional beam

Goose Bay beam 4 points poleward and represents a good example of a meridional beam (shown as a shaded green beam in Fig. 2). Figure 4a presents the velocity distribution for this beam, as well as the distribution in range gate-velocity space, for the whole of 1998. As with the zonal beam, the distribution displays a clear peak at zero. However, this distribution displays no other obvious occurrence maxima; a shoulder in the distribution at low negative velocities represents the only other significant feature. Figure 4b presents the same Goose Bay beam 4 velocity distribution but here, the contour map represents the distribution in magnetic local time-velocity space. What is immediately clear from Figs. 4a and 4b is that this meridional beam example shows no obvious signs of the far range E-region backscatter prevalent in the Iceland East beam 13 statistics, i.e. there are no discrete velocity peaks at or above the ion-acoustic speed. This is most likely due to differences in the propagation of the radar signal due to the different look directions of these beams. However, it may not solely be a result of the beam geometry; the Iceland East and Goose Bay radars typically operate in different frequency ranges (10.1–10.7 MHz and 13.0–13.4/14.3–14.8 MHz, respectively). The lower frequencies of the Iceland East signal may make it more conducive to the measurement of E-region backscatter.

The bulk of the distribution in Figs. 4a and 4b represents observations of the twin-cell convection flow. At low ranges (low-latitudes) where the convection flow is weaker, the velocity distribution is narrower. At mid to far ranges, the distribution is wider. Figure 4b confirms that these stronger flows relate predominantly to poleward flows in the noon sector and equatorward flows in the midnight sector, as expected during intervals of southward interplanetary magnetic field (during which most backscatter is observed). On top of this distribution there exists a sharper, highly symmetric peak, very close to zero, which most likely represents unflagged ground backscatter. Most of this ground backscatter occurs on the dayside (09:00–20:00 MLT) and as with the ground backscatter observed by Iceland East beam 13, the bulk of this backscatter occurs for $V_{los} < 35$ m/s.

Similar statistics to those shown in Figs. 3 and 4 were compiled for other beams from the SuperDARN radars in order to identify the possible sources of contamination in the different radars. Very low velocity echoes, suggestive of ground backscatter, were evident in all of the distributions (both in the zonal and meridional beams), but predominantly for $V_{los} < 35$ m/s. Discrete velocity peaks, suggestive of type I E-region backscatter, were evident in beams with a greater zonal component (the multiple discrete velocity peaks, were only obvious in the Iceland East zonal beams). Having identified the existence of potentially contaminating backscatter in the SuperDARN data set, we need a method to identify this backscatter in specific event data sets and to assess how it is processed by the mapping technique. We also needed to determine a method to optimise its removal, and to allow the production of more reliable global convection maps.

3 Assessing the impact of backscatter contamination – a case study

On 11 February 1998, four of the Northern Hemisphere SuperDARN radars (those shown in Fig. 2) observed backscatter during an interval where the interplanetary magnetic field B_z component was constantly negative, whilse the B_y component was close to zero. Figure 5 presents line-of-sight velocity data from sample beams from each of these four radars on this day illustrating the typical extent of the backscatter measured. In Fig. 5, the grey regions represent areas where the data have been flagged as ground backscatter by the SuperDARN raw data processing algorithm. Although there are extensive regions identified as ground backscatter during this interval, there are also large regions which are identified as ionospheric backscatter. The vertical dotted lines in Fig. 5 delineate the interval 13:00–14:16 UT, which corresponds to the $B_z < 0$ interval discussed above. It is this interval which forms our case study. At this time, the Goose Bay/Iceland West radar pair were observing the noon sector and the Finland/Iceland East (CUTLASS) radar pair were observing the afternoon/dusk sector.

3.1 Noon sector

Figure 5a presents V_{los} data from Goose Bay beam 4. Most of these data are identified as ionospheric backscatter, although there is a band of backscatter at ranges of $\sim$2000 km ($\sim$range gate 40) which is partially identified as ground backscatter. The very low velocities of the "ionospheric" backscatter in this same region are suggestive of a misidentification of this backscatter. A similar scenario exists in Figs. 5b, 5c and 5d. There are clear regions of ionospheric backscatter, characterised by large velocities, but also large regions identified as ground backscatter interspersed with low velocity "ionospheric" backscatter. These data sets are very typical for the Northern Hemisphere radars. We suggest that this low velocity backscatter almost certainly represents ground backscatter, possibly with an artificially enhanced spectral width, resulting from a combination of propagation modes (Barthes et al., 1998). We can confirm our hypothesis by studying the range gate-velocity distributions and elevation angle information for this interval.

Figure 6a presents the velocity distribution of data from all beams of the Goose Bay radar during the interval 13:00–14:16 UT, as well as a map of the distribution in range gate-velocity space. Figure 6b presents the distribution in elevation angle-range gate space, as well as a representation of the average velocity measured in each cell of the distribution. Elevation angle estimates cannot be made for all backscatter measurements and these are assigned an elevation angle of zero. The large band of samples at zero in Fig. 6b illustrates the extent to which elevation angle estimations could not be

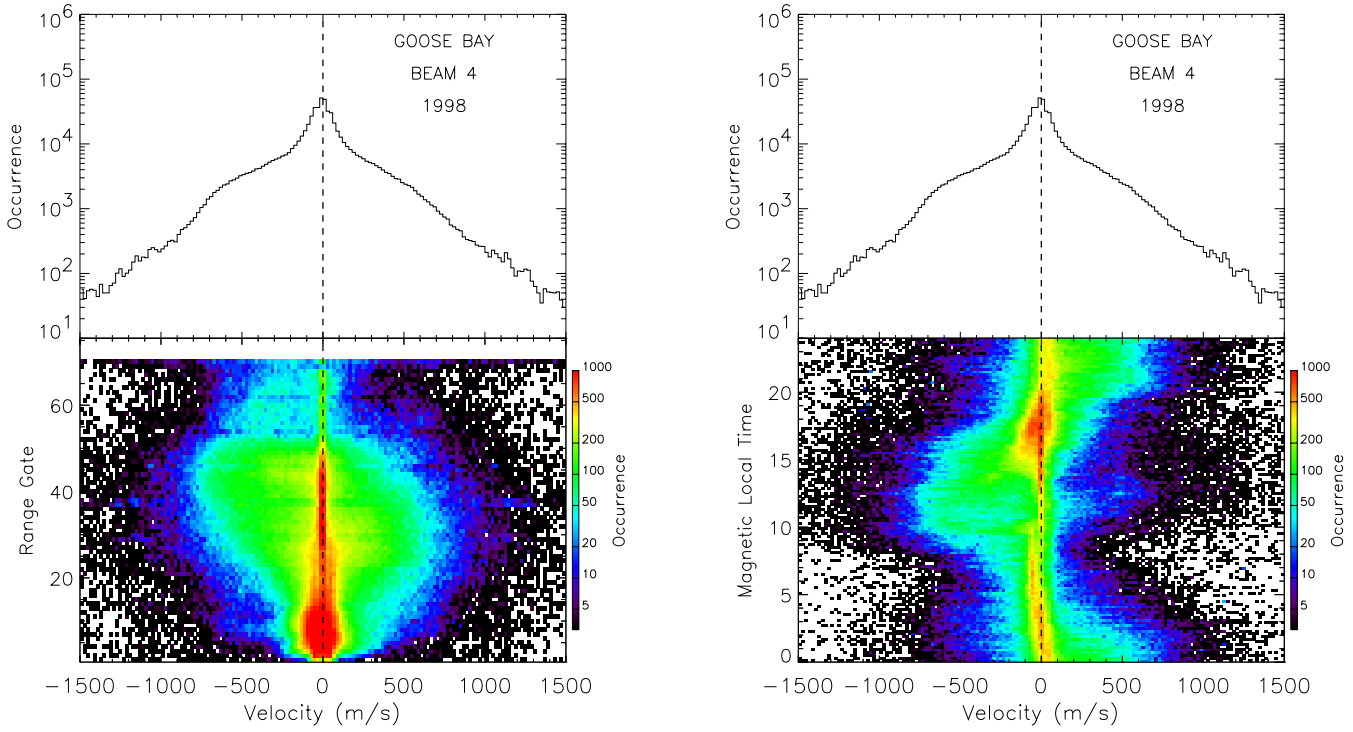

Fig. 4. Line-of-sight velocity distributions from Goose Bay beam 4 for the whole of 1998. Additionally shown are **(a)** the distribution in range gate-velocity space, and **(b)** the distribution in magnetic local time-velocity space. Positive line-of-sight velocities represent the flow toward the radar, whereas negative line-of-sight velocities represent the flow away from the radar.

made. Although the velocity distribution in Fig. 6a appears continuous, the two-dimensional maps clearly show the occurrence of four distinct distributions in the data set. The solid orange lines in Fig. 6b approximately delineate the four distributions.

First, there exists a small distribution at very low ranges, with low velocities and low elevation angles. This distribution appears to represent type II E-region backscatter. This E-region backscatter moves only under the influence of the convection electric field and does not, therefore, represent a potential source of contamination in the global convection maps. Second, a large distribution of points extends from low negative velocities at low ranges, to higher negative velocities at mid-ranges. This distribution represents the large region of F-region ionospheric backscatter, evident at low to mid-ranges in Fig. 5a. The large spread of this distribution in range gate-elevation angle space most likely results from the multitude of propagation modes which may exist during this interval due to spatial and temporal changes in the ionospheric density distribution and the combination of 16 beam look directions. Third, a small distribution of measurements exists at far ranges with high negative velocities. This region relates to the small regions of sporadic ionospheric backscatter seen at far ranges in Fig. 5a, and probably represents $1\frac{1}{2}$ hop F-region backscatter. Finally, a distribution at mid-ranges occurs exclusively at low velocities and is highly symmetric about the zero velocity. This distribution displays similar elevation angles to the F-region and multiple hop backscatter, suggesting that these modes have similar propagation paths. The range of this distribution is located between the two regions of ionospheric backscatter, at double the range of the $\frac{1}{2}$ hop F-region backscatter, suggesting that it represents a region of ground backscatter. This distribution also represents the region of backscatter partially identified as ground backscatter in Fig. 5a. We can, therefore, state with some confidence that this distribution represents ground backscatter which has not been identified as such during the raw data processing, and hence, is a potential source of contamination to the convection maps. There is no obvious sign of type I E-region backscatter in the Goose Bay data.

In order to produce reliable convection maps for this interval, we need to assess how this region of ground backscatter affects the convection mapping. First, we need to determine the effect that the gridding process (the preprocessing before the least-squares fit) has on the velocity distribution. Figure 7a shows in a format similar to the lower panel of Fig. 6a, the velocity distribution for this interval after default gridding of the data. The equivalent ground range (in km) represents the distance from the radar site to the centre of the relevant grid cell (see Ruohoniemi and Baker, 1998 for details of the grid cell geometry). The two panels show the occurrence distribution in range-velocity space (as in Fig. 6a), and the associated average velocity error in each cell of the distribution. It is the velocity error which determines the weighting of the measurement in a particular grid cell. It is clear (despite the change in range resolution) that the grid-

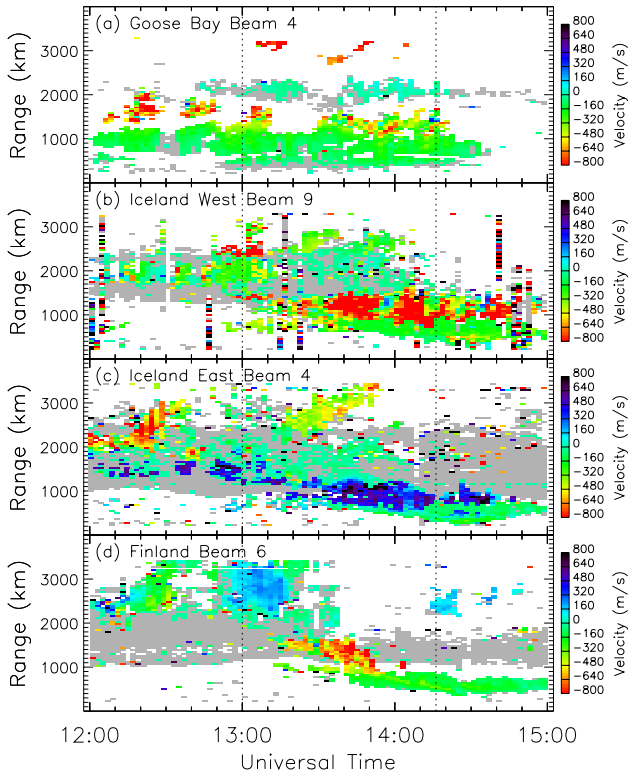

Fig. 5. Line-of-sight velocity measurements for the interval 12:00–15:00 UT on 11 February, 1998. The data are from **(a)** Goose Bay Beam 4, **(b)** Iceland West Beam 9, **(c)** Iceland East Beam 4, and **(d)** Finland Beam 6. The grey regions represent data flagged as ground backscatter by the SuperDARN raw data processing algorithm. Positive line-of-sight velocities represent the flow toward the radar, whereas negative line-of-sight velocities represent the flow away from the radar.

ded data (Fig. 7a) match closely the line-of-sight velocity input (Fig. 6a). It is also clear that the gridding process has effectively removed much of the noise in the distribution. Although largely reduced, the ground backscatter distribution still remains (∼1700–2300 km equivalent ground range), and most important, it is characterised by a low velocity error which implies that it will have a significant weighting in the fitting process. This ground backscatter will, therefore, significantly contaminate the resulting convection map.

Our problem is to find the most efficient method of removing the contaminating ground backscatter distribution. By increasing the minimum absolute velocity filter setting to ∼100 m/s in the gridding process, all the observed ground backscatter distribution would be removed. However, this would also remove a large section of the ionospheric backscatter distribution evident at lower ranges. A more efficient solution is to use a velocity-range gate filter to remove all the backscatter within a selected region of range gate-velocity space. The orange rectangle in Fig. 6a illustrates the extent of such a filter that contains only the ground backscatter distribution. Applying this filter to the data appears to be the optimum way of removing the unwanted ground backscatter distribution. Fig. 7b illustrates the effect of this filter on the gridded velocity data. The contaminating ground backscatter distribution has been completely removed from the data set.

In Fig. 8, we present a single scan comparison of the gridded velocity data as determined using the default processing, and using the velocity-range gate filtering. The figure presents two-dimensional V_{los} maps (in geomagnetic coordinates) from the Goose Bay and Iceland West radars for the interval 14:00–14:02 UT. Figure 8a presents the line-of-sight velocity data as measured by the Goose Bay radar. The grey regions represent backscatter that has been flagged as ground backscatter. The ground backscatter at mid-ranges (between ∼75° and 85° latitude), is interspersed with low velocity backscatter which relates to the misidentified ground backscatter distribution highlighted in Fig. 6. Figure 8b presents the gridded velocity data and illustrates the effect of the default preprocessing within the gridding process, namely the median filtering and the removal of all backscatter with $|V_{los}| < 35$ m/s. The gridded velocity data, as shown in Fig. 8b, encompass data from three consecutive scans of the sort shown in Fig. 8a. The gridding process removes all the noise from the data set and smoothes the data considerably. Although the default processing removes some of the ground backscatter, a large percentage remains (between ∼75° and 85° latitude). Figure 8c presents the gridded velocity data, after velocity-range gate filtering, using the filter described in Fig. 6. In this case, all the ground backscatter at mid-ranges (between ∼75° and 85° latitude) is removed. Figures 8d, 8e and 8f present the same figures for the Iceland West radar at this time. Velocity-range gate filters for this radar have been chosen by examining the associated range gate-velocity space and elevation angle distributions for the Iceland West radar (not shown). By comparing Figs. 8d and 8e, it is clear that the default processing removes some of the ground backscatter evident in Fig. 8d; the addition of the velocity-range gate filtering in Fig. 8f does make some difference to the gridded data.

We now examine how the differences between the default processing (as shown in Figs. 8b and 8e) and the velocity-range gate filtering (as shown in Figs. 8c and 8f) affect the convection map determined for this interval. Figure 9 presents noon-sector views of the global convection map for this interval (14:00–14:02 UT) in geomagnetic coordinates, using (a) the default processing, and (b) the velocity-range gate filtering. These convection maps have been produced using a high order fit (order 11) to accentuate mesoscale features of the map. The solid (dashed), red lines in this figure represent the equipotential contours of the global convection electric field solution in the afternoon (morning) convection cell. The bold, black dashed line represents the location of magnetic local noon. The magnitude of the velocity vectors is illustrated by the colour bar. Although much of the solution is very similar in the two cases, the unidentified ground backscatter distribution (evident between ∼76° and ∼83° latitude in Fig. 9a) significantly affects the convection map. The ground backscatter has produced a spurious mesoscale

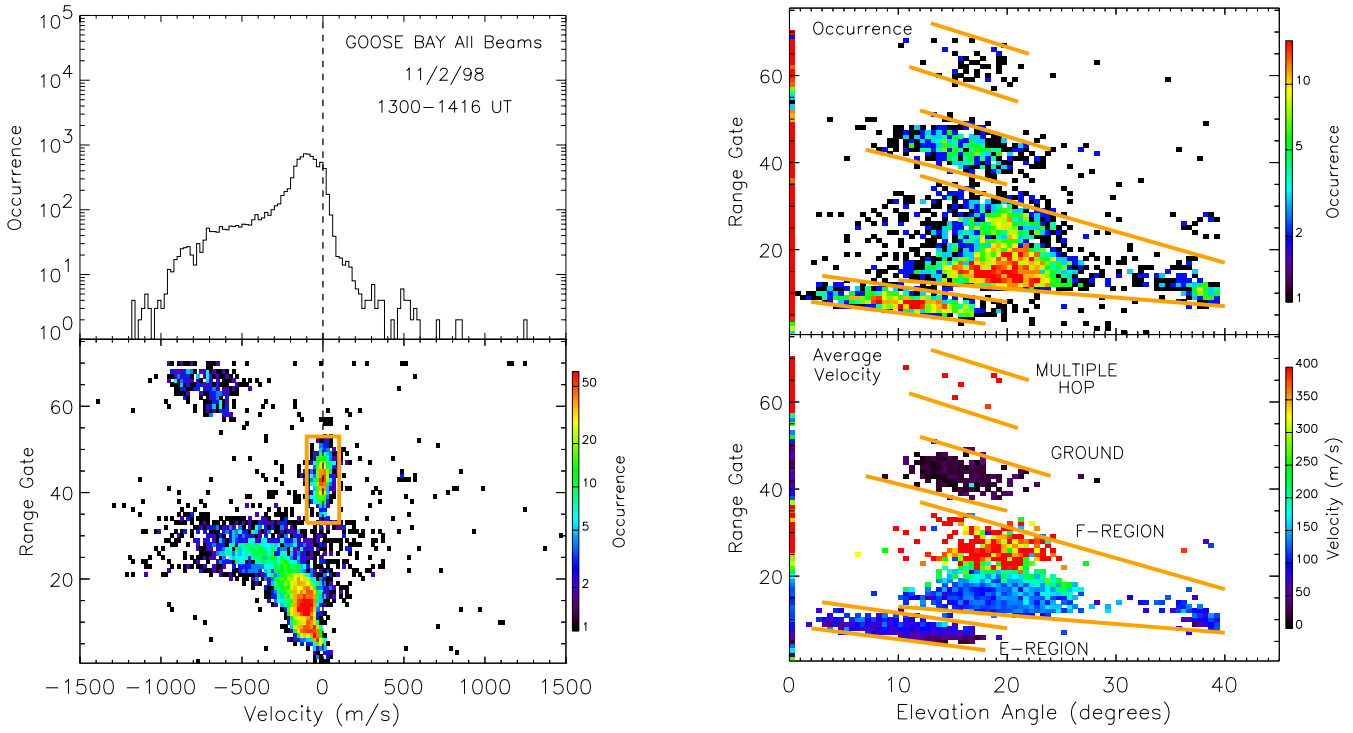

Fig. 6. (a) Line-of-sight velocity distribution from all beams of the Goose Bay radar for the interval 13:00–14:16 UT on 11 February 1998, as well as the distribution in range gate-velocity space. The orange rectangle represents the extent of the velocity-range gate filter applied to these data to remove contaminating ground backscatter. **(b)** Occurrence distribution for the same interval in range gate-elevation angle space, as well as the average line-of-sight velocity measured in each distribution cell.

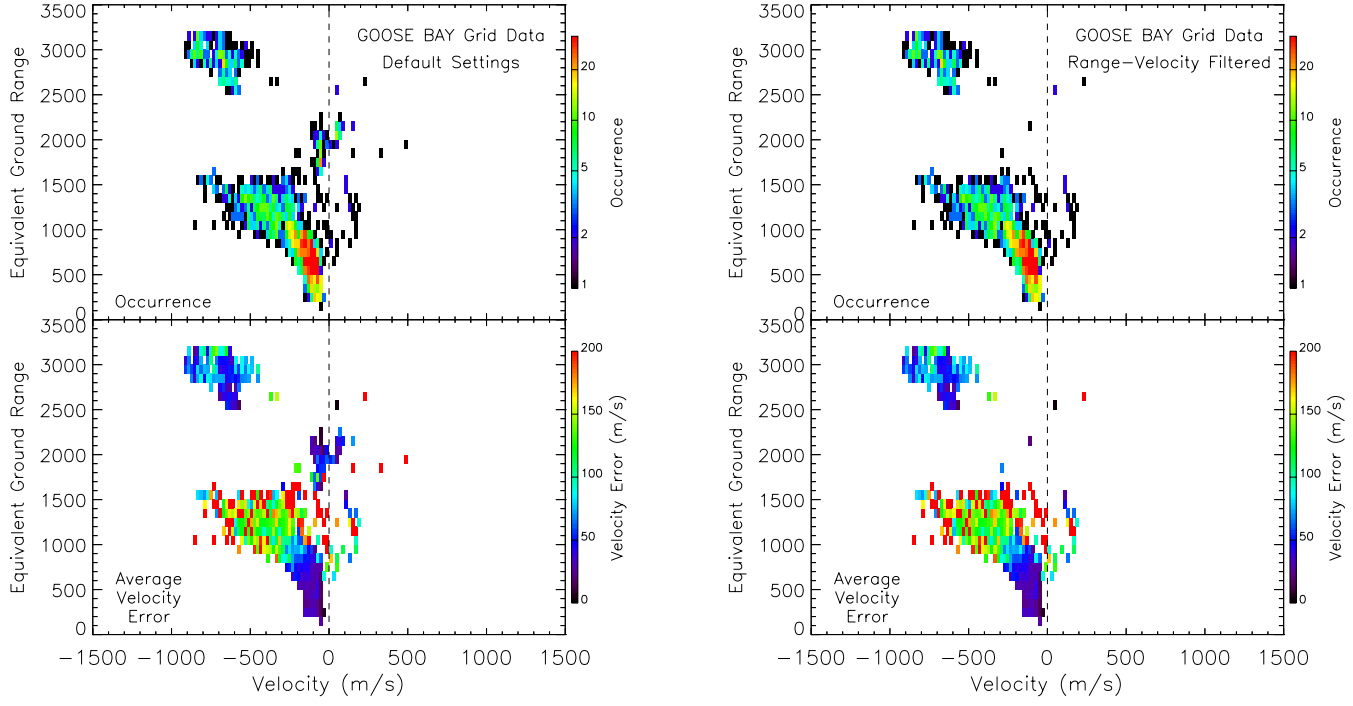

Fig. 7. Gridded velocity distribution from the Goose Bay radar for the interval 13:00–14:16 UT on 11 February 1998, using **(a)** the default processing, and **(b)** velocity-range gate filtering. Also shown is the average velocity error measured in each distribution cell.

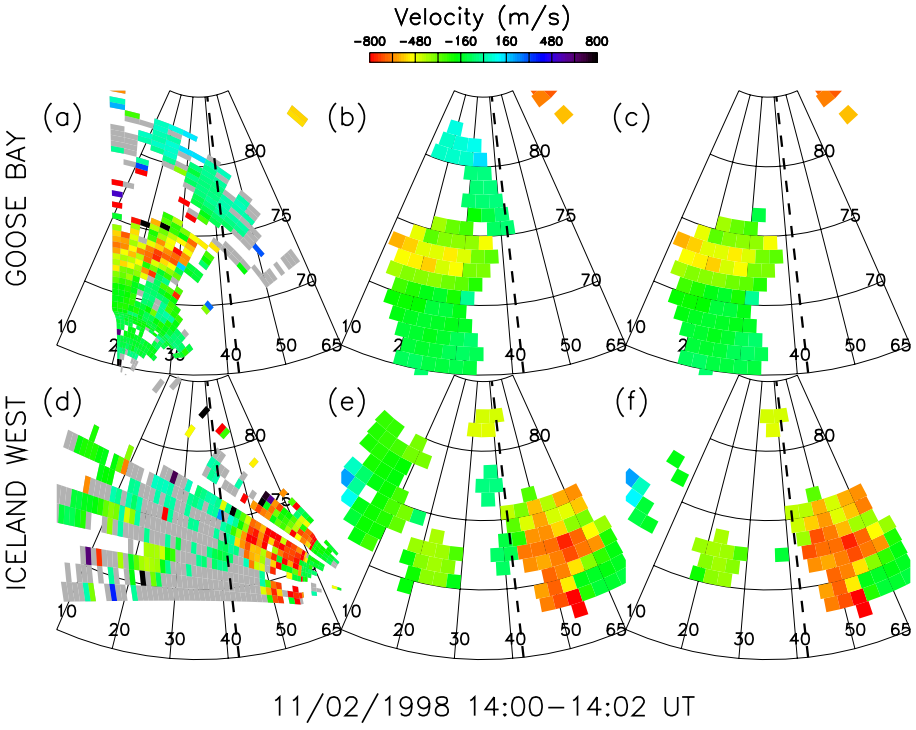

Fig. 8. Line-of-sight velocity map in geomagnetic coordinates for a single scan interval on 11 February 1998, (14:00–14:02 UT) for: **(a)** Goose Bay – the grey region represents data identified as ground backscatter by the raw data processing. **(b)** Goose Bay – gridded velocity data using default processing. **(c)** Goose Bay – gridded velocity data using velocity-range gate filtering. **(d)** Iceland West – the grey region represents data identified as ground backscatter by the raw data processing. **(e)** Iceland West – gridded velocity data using default processing. **(f)** Iceland West – gridded velocity data using velocity-range gate filtering. The bold dashed lines represent the location of magnetic local noon.

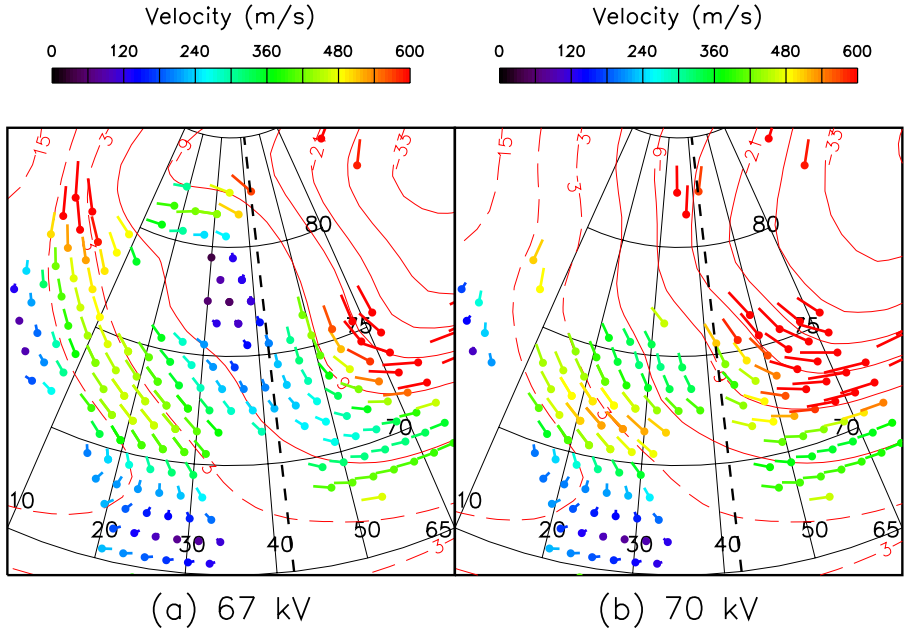

Fig. 9. Comparison of global convection map features in the noon sector in geomagnetic coordinates for the interval 14:00–14:02 UT on 11 February 1998, representing **(a)** default processing, and **(b)** velocity-range gate filtering. The arrows represent the flow determined from the global convection mapping solution at grid points where data were entered. The solid (dashed), red lines represent equipotentials of the estimated convection electric field for the afternoon (morning) convection cell. The bold, dashed line represents the location of magnetic local noon.

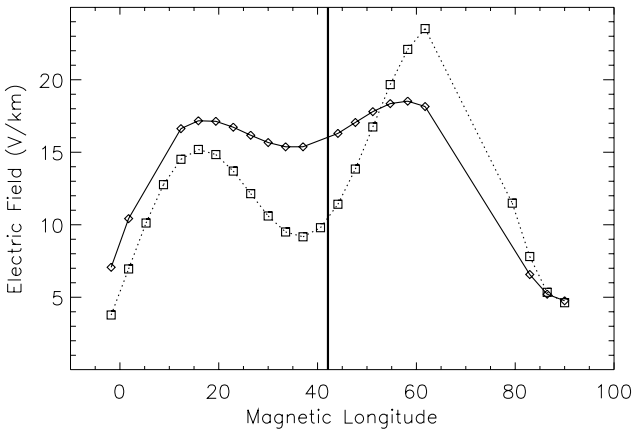

Fig. 10. Longitudinal (MLT) variation of the zonal component of the convection electric field at 73.5° geomagnetic latitude determined from the global convection mapping technique for the interval 14:00–14:02 UT on 11 February 1998. The dotted line represents the variation obtained from using the default processing (as in Figure 9a), whereas the solid line represents the variation obtained from using velocity-range gate filtering (as in Fig. 9b).

feature (almost a null point in the convection flow), which severely distorts the equipotential contours of the electric field. Null points have been observed to occur naturally in legitimate observations of the ionospheric convection flow (Morelli et al., 1995) and hence, the correct identification of mesoscale features, such as that shown in our example, is of crucial importance.

The contaminating backscatter is also affecting the solution at lower latitudes. Figure 10 presents the zonal component of the convection electric field (equivalent to the meridional component of the convection flow) at 73.5° geomagnetic latitude, determined from the solutions of the global convection mapping displayed in Figs. 9a and 9b. The dotted line represents the solution shown in Fig. 9a which includes the region of ground backscatter, and the solid line represents the solution shown in Fig. 9b where this contaminating backscatter has been removed by velocity-range gate filtering. The bold vertical line in Fig. 10 represents the location of magnetic local noon at this time. The dotted line in Fig. 10 shows a clear drop in the zonal electric field close to noon, related to the spurious null region in the flow, giving the illusion that the zonal electric field in the noon sector is concentrated in two peaks on either side of noon. The solid line shows that once this contamination is removed, this feature is largely reduced, and that the zonal electric field is approximately constant across magnetic local noon.

Although this contaminating backscatter appears to have significantly altered the features at the mesoscale level, large-scale characteristics of the solution, such as the cross-polar cap potential (67 kV and 70 kV for Figs. 9a and 9b, respectively), are relatively unchanged. However, this may simply be a result of model data dominating the global solution when the global data coverage is not extensive in both convection cells.

3.2 Dusk sector

Figure 11a presents the velocity distribution for all beams from the Iceland East radar for the same interval as discussed above (13:00–14:16 UT), as well as a map of the distribution in range gate-velocity space. Figure 11b presents the distribution in elevation angle-range gate space, as well as a representation of the average velocity measured in each distribution cell. The backscatter distribution for this radar is more complicated (and noisier) than that for the Goose Bay radar during this interval (as shown in Figs. 6a and 6b). The elevation angle information in particular is highly complex and open to a number of interpretations; there appears to be significant overlap of propagation modes in elevation angle-range gate space. However, as with the Goose Bay data, a number of distinct distributions can be identified in the data and these are approximately delineated by the solid orange lines in Fig. 11b.

First, similar to the Goose Bay distribution, but extending across a larger number of range gates, is a large, low velocity distribution symmetric about zero, coincident with the large region identified predominantly as ground backscatter in Fig. 5c. As with the Goose Bay data, this almost certainly represents contaminating ground backscatter and can be removed effectively by applying the velocity-range gate filter which is shown as an orange rectangle in Fig. 11a. The overlap of propagation modes means that the average velocity in this region of elevation angle-range gate space is not always as low as that expected from a ground backscatter distribution. Second, at far ranges, is a narrow velocity distribution centred at ~ -400 m/s. This backscatter distribution resembles the type I E-region backscatter which is constrained to the ion-acoustic speed, as shown in Fig. 3a, and is clearly a multiple-hop propagation mode. The lack of convection associated backscatter at far ranges in Fig. 3a would appear to support this interpretation. Hence, this may also represent a potential source of contamination to the global convection maps. However, there is also the possibility that this backscatter is convection related. Interestingly, also at far ranges are small, discrete velocity distributions at ± 850 m/s and +400 m/s which resemble the discrete velocity peaks presented in Fig. 3a. We cannot be completely confident that any of these data at these far ranges are solely convection related, and hence, one option is to remove all V_{los} data beyond a selected range gate (as shown by the horizontal orange line in Fig. 11a). We will assess the advantages and disadvantages of removing this "suspected" E-region backscatter later in this section. Third, at low to mid-ranges, a distribution exists extending from low to high velocities. The extent of this distribution and its location in elevation angle-range gate space suggests that it represents ionospheric F-region backscatter. Finally, at low ranges, there is a low velocity distribution which appears to represent type II E-region backscatter.

As with the noon-sector case, it is important to assess the effect of the gridding process on the velocity distribution. Figure 12a shows (in the same format as Fig. 7a) the velocity distribution from the Iceland East radar after default

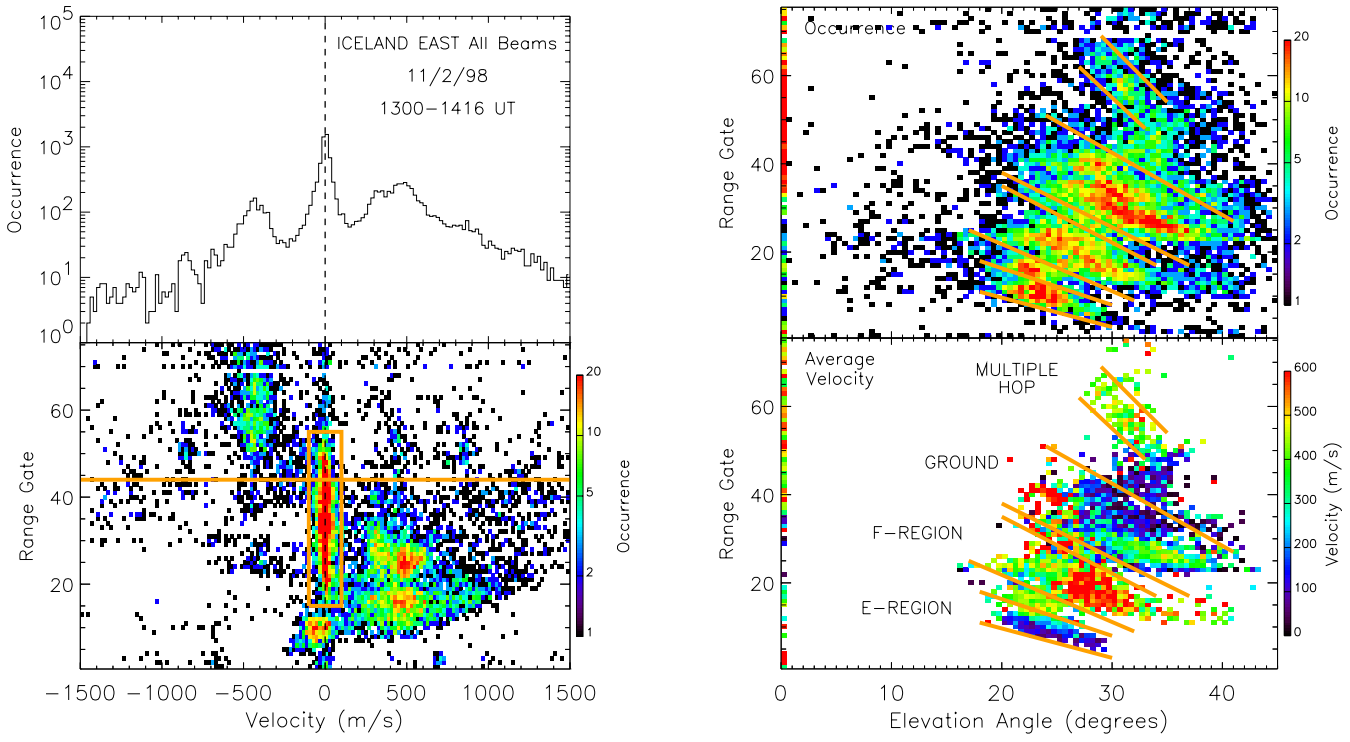

Fig. 11. (a) Line-of-sight velocity distribution from all beams of the Iceland East radar for the interval 13:00–14:16 UT on 11 February 1998, as well as the distribution in range gate-velocity space. The orange rectangle represents the extent of the velocity-range gate filter applied to these data to remove contaminating ground backscatter. The horizontal orange line represents the range gate above which all data have been removed to eliminate possible contaminating E-region backscatter. **(b)** Occurrence distribution for the same interval in range gate elevation angle space, as well as the average velocity measured in each distribution cell.

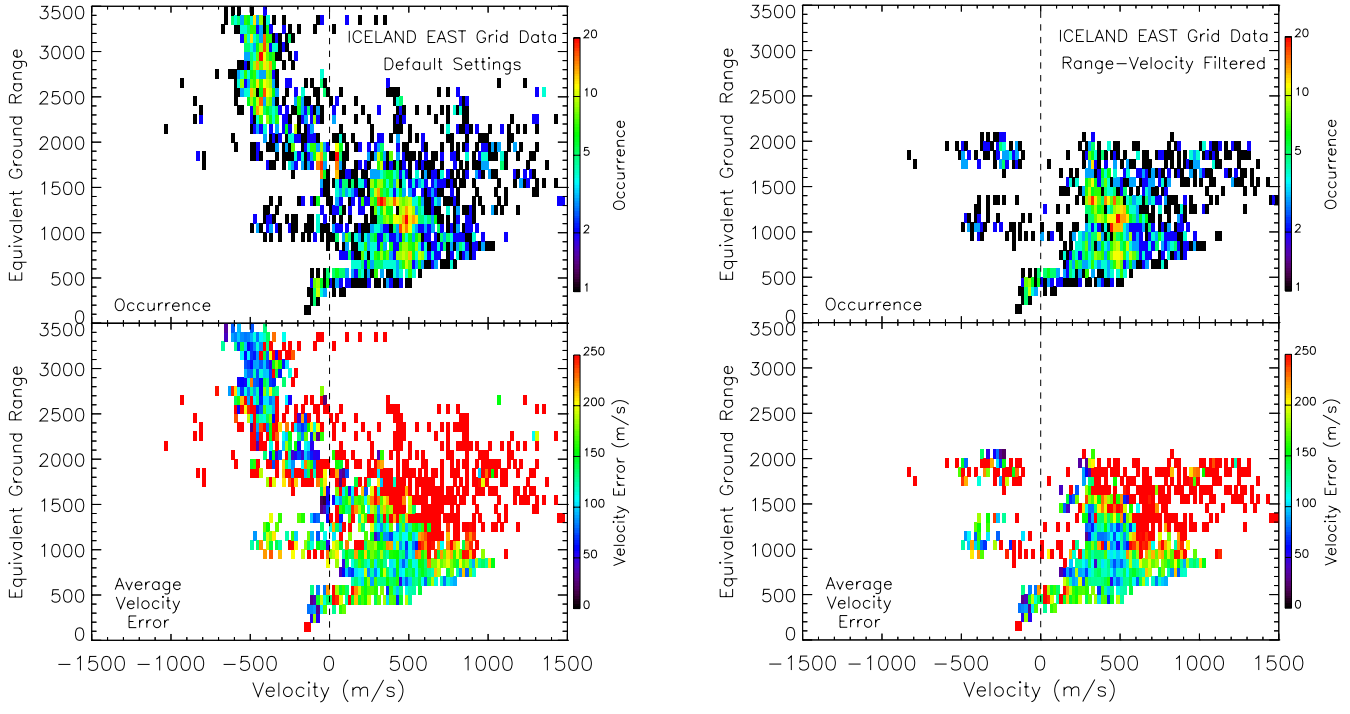

Fig. 12. Gridded velocity distribution for the Iceland East radar for the interval 13:00–14:16 UT on 11 February 1998, using **(a)** the default processing, and **(b)** velocity-range gate filtering. Also shown is the average velocity error measured in each distribution cell.

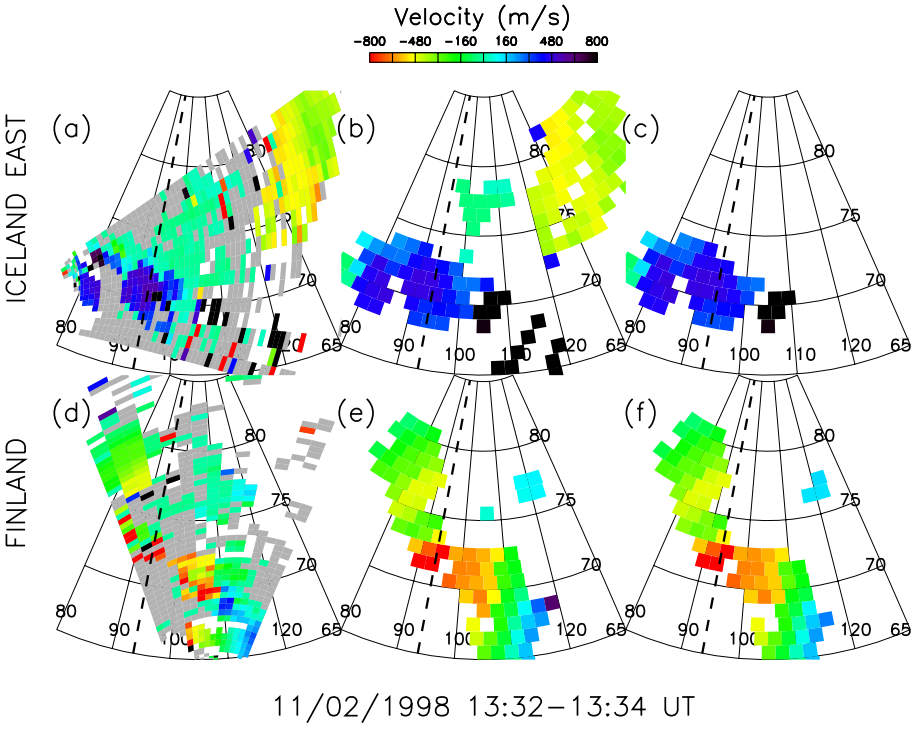

Fig. 13. Line-of-sight velocity map in geomagnetic coordinates for a single scan interval on 11 February 1998, (13:32–13:34 UT) for: **(a)** Iceland East - the grey region represents data identified as ground backscatter by the raw data processing. **(b)** Iceland East - gridded velocity data using default processing. **(c)** Iceland East - gridded velocity data using velocity-range gate filtering. **(d)** Finland - the grey region represents data identified as ground backscatter by the raw data processing. **(e)** Finland - gridded velocity data using default processing. **(f)** Finland - gridded velocity data using velocity-range gate filtering. The bold, dashed lines represent the location of 15:00 MLT.

gridding of the velocity data. The distribution still appears quite noisy, even after the median filtering of the data within the gridding process. However, much of the "noisy" part of the distribution, where the occurrence rates are low, is characterised by a large velocity error. This data will be significantly down-weighted in the fitting process and will, therefore, have a minimal impact on the resulting convection map. However, it is clear from Fig. 12a that much of the ground backscatter distribution remains after the default processing, as does the suspected region of type I E-region backscatter at far ranges. This region is characterised by a low velocity error and hence, will have a significant weighting in the fitting process. Figure 12b illustrates the effect of applying the two range gate-velocity filters shown in Fig. 11a. The potential contaminating backscatter distributions have been largely removed from the gridded velocity data set.

In Fig. 13, we present a single scan comparison of the gridded velocity data as determined using the default processing, and after applying the two velocity-range gate filters. The figure presents two-dimensional V_{los} maps from the Iceland East and Finland radars for the interval 13:32–13:34 UT. The breakdown of this figure is exactly the same as that used for the Goose Bay and Iceland West maps shown in Fig. 8, except that the bold dashed line now represents 15:00 MLT. Figure 13a shows a large distribution of very low velocity backscatter which has not been identified as ground backscatter by the raw data processing. However, the default processing applied by the gridding process removes much of this ground backscatter, as shown in Fig. 13b. However, a small amount of ground backscatter remains at low to mid-ranges (∼75–79° latitude). Figure 13c shows the result of applying the two velocity-range gate filters illustrated in Fig. 11a. The application of one of these filters has completely removed the region of ground backscatter at low to mid-ranges. The other filter has resulted in the removal of the large region of backscatter at far ranges. This region of backscatter is the multiple-hop backscatter suspected of being type I E-region backscatter in Fig. 11. Figures 13d, 13e and 13f present the same figures for the Finland radar at this time. In this case, the default processing (Fig. 13e) removes the bulk of the ground backscatter evident in Fig. 13d. The velocity-range gate filters (Fig. 13f) remove little other backscatter.

We need to assess the affect of this contamination on the convection maps and hence, we compare the default convection map with that determined after the removal of the ground backscatter only, and that determined after the removal of both the ground and suspected E-region backscatter. Figure 14 presents a dusk sector view of the global convection map for this interval using (a) the default processing (as shown in Figs. 13b and 13e), (b) the ground backscatter velocity-range gate filter only, and (c) both velocity-range gate filters (as shown in Figs. 13c and 13f). This figure has

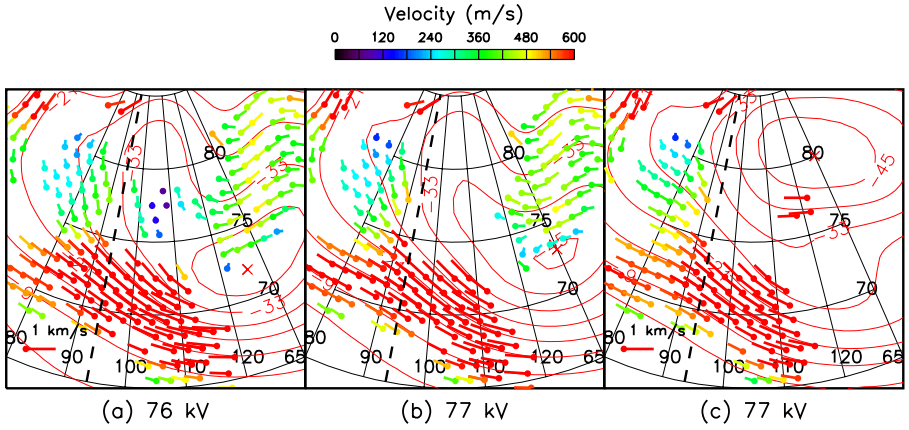

Fig. 14. Comparison of global convection map features in the dusk sector in geomagnetic coordinates for the interval 13:32–13:34 UT on 11 February 1998, representing **(a)** default processing, **(b)** velocity-range gate filtering to remove ground backscatter, and **(c)** velocity-range gate filtering to remove both ground and far-range E-region backscatter. The arrows represent the flow determined from the global convection mapping solution at grid points where data were entered. The solid (dashed), red lines represent equipotentials of the estimated convection electric field for the afternoon (morning) convection cell. The bold, dashed line represents the location of 15:00 MLT.

the same format as Fig. 9; the bold dashed line represents the location of 15:00 MLT. The convection maps shown in Figs. 14a and 14b are very similar, and the removal of the ground backscatter has not made a significant difference. However, it is obvious that there are significant differences between these maps and that shown in Fig. 14c. The removal of the far range backscatter, suspected of being type I E-region backscatter, from the Iceland East data has radically changed the morphology of the afternoon convection cell, both in its shape and position. Most significantly, the centre of the afternoon convection cell has moved from ∼72° to ∼80° in latitude. However, it must be stressed that the regions of the convection pattern where data have been removed represent an unreliable solution since they are conditioned only by model velocity vectors. The solution can only be considered wholly reliable where good data exist.

In order to assess the relative reliability of these convection maps, we have studied data from a DMSP-F13 Northern Hemisphere pass (M. R. Hairston, private communication) at ∼13:30 UT, which clearly places the convection reversal boundary at 72° geomagnetic latitude at 16:30 MLT. This matches the convection scenario presented in Fig. 14b, before the removal of the suspected E-region backscatter. We conclude from this analysis that although the velocity of the E-region backscatter is not solely convection related, this backscatter does accurately constrain the flow direction within the polar cap where there is little other data, and it allows us to reliably set the convection reversal boundary. This part of the solution should still be viewed with caution however; although the overall direction of the vectors in this region may be reliable, the magnitude of these vectors may be significantly underestimated due to the limiting of the velocity of the type I E-region backscatter to near the ion-acoustic speed. It should also be noted that the significant mesoscale changes in the convection pattern shown under various assumptions in Fig. 14, again have little effect on the global cross-polar cap potential (76 kV, 77 kV, and 77 kV for Figs. 14a, 14b and 14c, respectively).

4 Summary

Although contamination from non-F-region backscatter does not usually have a significant effect on the global characteristics of ionospheric convection determined using the SuperDARN global convection mapping method (e.g. the magnitude of the cross-polar cap potential), we have shown that it can greatly affect mesoscale features of the solution e.g. the structure of flow vortices, convection reversal boundaries, and flow transients. Hence, it is crucially important when using SuperDARN global convection mapping in the study of mesoscale features of this sort, to identify the extent of possible contaminating backscatter in the data set and understand its influence on the electric field solution. Failure to do so could result in the identification of spurious convection features and lead to misinterpretation of the data.

The global convection mapping default gridding process removes much of the ground backscatter recorded by the radars, but can still leave a significant percentage, which can result in spurious mesoscale variations in the convection maps. At present, the gridding process does not attempt to remove type I E-region backscatter, which we have shown is prevalent in zonal-pointing SuperDARN radar beams (normally under the auroral oval). Although, as we have shown, removing this E-region backscatter may not always result in a more accurate convection map. Inspection of the distribution of data in range gate-velocity space and range gate-elevation angle space can highlight potential contaminating backscatter distributions. The application of a series of suitable velocity-range gate filters during the gridding process can remove any unwanted backscatter. This solution is also

applicable to the determination of convection velocity vectors using the "merge" technique; the "merge" default minimum velocity of 25 m/s is insufficient to remove all ground backscatter, resulting in the possibility of erroneous merged vectors. Although velocity-range gate filtering represents an adequate solution to these problems, in the long-term a more objective and automatic solution which combines velocity, spectral width, range gate, and elevation angle information is desirable.

Acknowledgements. We would like to thank the principal investigators of the SuperDARN radars used in this study; R. Greenwald for Goose Bay, J.-P. Villain for Iceland West (Stokkseyri), and M. Lester for Iceland East (CUTLASS Iceland) and Finland (CUTLASS Finland). CUTLASS is supported by the Particle Physics and Astronomy Research Council, UK, the Swedish Institute for Space Physics, Uppsala, and the Finnish Meteorological Institute, Helsinki. Support for the Goose Bay radar is provided in part by the NSF and in part by NASA. Support for the Stokkseyri radar is provided by the CNRS/INSU. We would also like to thank M. P. Freeman and A. S. Rodger for helpful discussions.

Topical Editor M. Lester thanks G. Provan and another referee for their help in evaluating this paper.

References

Amm, O., Engebretson, M. J., Greenwald, R. A., Lühr, H., and Moretto, T.: Direct determination of IMF B_y-related cusp current systems, using SuperDARN radar and multiple ground magnetometer data: A link to theory on cusp current origin, J. Geophys. Res., 104, 17 187–17 198, 1999.

André, D., Sofko, G. J., Baker, K., and MacDougall, J.: SuperDARN interferometry: Meteor echoes and electron densities from groundscatter, J. Geophys. Res., 103, 7003–7015, 1998.

Baker, K. B., Dudeney, J. R., Greenwald, R. A., Pinnock, M., Newell, P. T., Rodger, A. S., Mattin, N., and Meng, C.-I.: HF radar signatures of the cusp and low-latitude boundary layer, J. Geophys. Res., 100, 7671–7695, 1995.

Barthes, L., André, R., Cerisier, J.-C., and Villain, J.-P.: Separation of multiple echoes using a high-resolution spectral analysis for SuperDARN HF radars, Radio Sci., 33, 1005–1017, 1998.

Buneman, O.: Excitation of field-aligned sound waves by electron streams, Phys. Rev. Lett., 10, 285–287, 1963.

Cerisier, J.-C. and Senior, C.: Merge: A FORTRAN program, Tech. rep., Centre d'Étude des Environnements Terrestres et Planétaires CNRS, 1994.

Davies, J. A., Lester, M., Milan, S. E., and Yeoman, T. K.: A comparison of velocity measurements from the CUTLASS Finland radar and the EISCAT UHF system, Ann. Geophysicae, 17, 892–902, 1999.

Eglitis, P., Robinson, T. R., Rietveld, M. T., Wright, D. M., and Bond, G. E.: The phase speed of artificial field-aligned irregularities observed by CUTLASS during HF modification of the auroral ionosphere, J. Geophys. Res., 103, 2253–2259, 1998.

Farley, D. T.: A plasma instability resulting in field-aligned irregularities in the ionosphere, J. Geophys. Res., 63, 6083–6097, 1963.

Farley, D. T., Sahr, J. D., and Providakes, J. F.: Ion-cyclotron harmonics in auroral radar echoes – real effect or analysis artifact, Geophys. Res. Lett., 18, 709–712, 1991.

Fejer, B. G. and Kelley, M. C.: Ionospheric irregularities, Rev. Geophys. Space Phys., 18, 401–454, 1980.

Fejer, B. G., Reed, R. W., Farley, D. T., Swartz, W. E., and Kelley, M. C.: Ion cyclotron waves as a possible source of resonant auroral radar echoes, J. Geophys. Res., 89, 187–194, 1984.

Greenwald, R. A., Baker, K. B., Dudeney, J. R., Pinnock, M., Jones, T. B., Thomas, E. C., Villain, J.-P., Cerisier, J.-C., Senior, C., Hanuise, C., Hunsucker, R. D., Sofko, G., Koehler, J., Nielsen, E., Pellinen, R., Walker, A. D. M., Sato, N., and Yamagishi, H.: DARN/SuperDARN: A global view of the dynamics of high-latitude convection, Space Sci. Rev., 71, 761–796, 1995.

Greenwald, R. A., Ruohoniemi, J. M., Baker, K. B., Bristow, W. A., Sofko, G. J., Villain, J.-P., Lester, M., and Slavin, J.: Convective response to a transient increase in dayside reconnection, J. Geophys. Res., 104, 10 007–10 015, 1999.

Haldoupis, C.: A review on radio studies of auroral E-region ionospheric irregularities, Ann. Geophysicae, 7, 239–258, 1989.

Haldoupis, C., Sofko, G. J., Koehler, J. A., and Danskin, D. W.: A new look at type 4 echoes of radar aurora, J. Geophys. Res., 96, 11 353–11 362, 1991.

Haldoupis, C., Koehler, J. A., Sofko, G. J., Danskin, D. W., McKibben, M. J., and André, D.: Preferential phase velocities for type 4 irregularities in the auroral E-region plasma, J. Geophys. Res., 98, 6173–6179, 1993.

Huang, C.-S., Sofko, G. J., Koustov, A. V., André, D. A., Ruohoniemi, J. M., Greenwald, R. A., and Hairston, M. R.: Evolution of ionospheric multicell convection during northward interplanetary magnetic field with $|B_z/B_y| > 1$, J. Geophys. Res., 105, 27 095–27 108, 2000.

Milan, S. E. and Lester, M.: Simultaneous observations at different altitudes of ionospheric backscatter in the eastward electrojet, Ann. Geophysicae, 16, 55–68, 1998.

Milan, S. E., Jones, T. B., Robinson, T. R., Thomas, E. C., and Yeoman, T. K.: Interferometric evidence for the observation of ground backscatter originating behind the CUTLASS coherent HF radars, Ann. Geophysicae, 15, 29–39, 1997a.

Milan, S. E., Yeoman, T. K., Lester, M., Thomas, E. C., and Jones, T. B.: Initial backscatter occurrence statistics from the CUTLASS HF radars, Ann. Geophysicae, 15, 703–718, 1997b.

Morelli, J. P., Bunting, R. J., Cowley, S. W. H., Farrugia, C. J., Freeman, M. P., Friis-Christensen, E., Jones, G. O. L., Lester, M., Lewis, R. V., Lühr, H., Orr, D., Pinnock, M., Reeves, G. D., Williams, P. J. S., and Yeoman, T. K.: Radar observations of auroral zone flows during a multiple-onset substorm, Ann. Geophysicae, 13, 1144–1163, 1995.

Neudegg, D. A., Cowley, S. W. H., Milan, S. E., Yeoman, T. K., Lester, M., Provan, G., Haerendel, G., Baumjohann, W., Nikutowski, B., Büchner, J., Auster, U., Fornacon, K.-H., and Georgescu, E.: A survey of magnetopause FTEs and associated flow bursts in the polar ionosphere, Ann. Geophysicae, 18, 416–435, 2000.

Nielsen, E. and Schlegel, K.: A first comparison of STARE and EISCAT electron drift velocity measurements, J. Geophys. Res., 88, 5745–5750, 1983.

Ossakow, S. L. and Chaturvedi, P. K.: Current convective instability in the diffuse aurora, Geophys. Res. Lett., 6, 332–334, 1979.

Prikryl, P., Sofko, G. J., Koehler, J. A., Mu, J., and André, D.: Steep electron density gradients associated with discrete aurorae explaining the diversity of auroral VHF Doppler spectra, Ann. Geophysicae, 13, 25–37, 1995.

Ruohoniemi, J. M. and Baker, K. B.: Large-scale imaging of high-latitude convection with Super Dual Auroral Radar Network HF

radar observations, J. Geophys. Res., 103, 20 797–20 811, 1998.

Ruohoniemi, J. M. and Greenwald, R. A.: Statistical patterns of high-latitude convection obtained from Goose Bay HF radar observations, J. Geophys. Res., 101, 21 743–21 763, 1996.

Ruohoniemi, J. M. and Greenwald, R. A.: Rates of scattering occurrence in routine HF radar observations during solar cycle maximum, Radio Sci., 32, 1051–1070, 1997.

Ruohoniemi, J. M., Greenwald, R. A., Baker, K. B., and Villain, J.-P.: Drift motions of small-scale irregularities in the high-latitude F-region: An experimental comparison with plasma drift motions, J. Geophys. Res., 92, 4553–4564, 1987.

Shepherd, S. G. and Ruohoniemi, J. M.: Electrostatic potential patterns in the high-latitude ionosphere constrained by SuperDARN measurements, J. Geophys. Res., 105, 23 005–23 014, 2000.

Shepherd, S. G., Greenwald, R. A., and Ruohoniemi, J. M.: A possible explanation for rapid, large-scale ionospheric responses to southward turnings of the IMF, Geophys. Res. Lett., 26, 3197–3200, 1999.

St.-Maurice, J.-P., Prikryl, P., Danskin, D. W., Hamza, A. M., Sofko, G. J., Koehler, J. A., Kustov, A., and Chen, J.: On the origin of narrow non-ion-acoustic coherent radar spectra in the high-latitude E-region, J. Geophys. Res., 99, 6447–6474, 1994.

Tsunoda, R. T.: High-latitude F-region irregularities: A review and synthesis, Rev. Geophys., 26, 719–760, 1988.

Villain, J.-P., Greenwald, R. A., and Vickrey, J. F.: HF ray tracing at high latitudes using measured meridional electron density distributions, Radio Sci., 19, 359–374, 1984.

Villain, J.-P., Caudal, G., and Hanuise, C.: A SAFARI-EISCAT comparison between the velocity of F-region small-scale irregularities and the ion drift, J. Geophys. Res., 90, 8433–8443, 1985.

Yeoman, T. K., Lewis, R. V., Khan, H., Cowley, S. W. H., and Ruohoniemi, J. M.: Interhemispheric observations of nightside ionospheric electric fields in response to IMF B_z and B_y changes and substorm pseudobreakup, Ann. Geophysicae, 18, 897–907, 2000.